© AUG 2023 | IRE Journals | Volume 7 Issue 2 | ISSN: 2456-8880
DOI: https://doi.org/10.64388/IREV7I2-1718338

Failure Modes and Deformation Patterns in 2D Sandwich Architected Materials Under Static and Dynamic Loading

BAMIDELE FADAYOMI
Department of Mechanical Engineering, Texas A&M University

Abstract- This study develops and executes a systematic experimental protocol for testing different variations of 2D honeycomb and diamond sandwich architected structures manufactured from UV-cured brittle photopolymer resin via additive manufacturing. Each sandwich structure was subjected to three loading conditions: local compression (3-point bending), uniform compression (quasi-static compression), and low-velocity impact loading, with five replicate specimens per combination. The research addresses four central questions: how do the tested lattices fail; what aspects of failure are reproducible; what effect does micro-architecture have on failure; and what are the differences between dynamic and static loading for these sandwich structures. The 2D architected structures were parametrically varied by changing a specific angle (θ) in their unit cell. For honeycomb, the angular variations were 15°, 30°, 45°, and functionally graded; for diamond, 45°, 90°, 120°, and functionally graded. Results show that core shear was the dominant failure mode across all honeycomb variations, while buckling dominated for the 45° and 90° diamond variations. The 120° and functionally graded diamond variations exhibited bending-dominated deformation with minimal fracture. Load responses under static loading conformed to Type II structural behaviour for honeycomb and the lower-angle diamond variations, and Type I behaviour for the 120° and functionally graded diamond configurations. Repeatable fracture and deformation patterns including 120° and 180° fracture path lines were identified across most variations. The 45° diamond variation demonstrated the highest strength and stiffness, while the 120° diamond variation showed the highest impact absorption. Functionally graded structures exhibited a notable tunability effect, enabling selective compliance in targeted core regions.

Keywords: Architected Materials, Sandwich Structures, Honeycomb, Diamond Lattice, Failure Modes, Additive Manufacturing, 3-Point Bending, Quasi-Static Compression, Low-Velocity Impact, Digital Image Correlation

I. INTRODUCTION

The use of architected materials has become more commonplace in structural design. More commonly, 2D architected sandwich plates have been employed in creating high-stiffness and lightweight parts used in aerospace, naval, automotive, and several other applications over the past two decades. In the past, manufacturing methods for sandwich structures required making each layer component separately and bonding them together. However, improvements in manufacturing processes have spurred the design of homogenous and more complex sandwich structures with unique mechanical properties [17], [18].

Today, several new types of core geometries ranging from 2D to 3D have been tested to understand their energy-related qualities [11]. However, there is still importance in exploring the failure modes of some fundamental core geometries used during the initial exploration of architected materials. It is interesting to understand how changes in the unit cell for each of these topologies can affect the overall performance of the structure. Two basic core geometries of interest are the honeycomb lattice in an in-plane orientation and the diamond-celled lattice [2], [4].

The term "architected materials" was first coined by Ashby and Brechet to link practices in architecture and engineering that develop light, stiff, and elegant structures. Better defined, an architected material is a combination of different materials, which could include open space, configured to reach performances that cannot be achieved by any of the individual materials [13], [14], [8], [9]. While much research focuses on the force-displacement response and energy absorption capabilities of architected materials, there is comparatively little known about the ways they fracture. It is, therefore, essential to study the behaviours of these structures to better understand and predict how they fail   information that is essential for proper validation of simulation results.

This study investigates the following research questions:

(i) How do honeycomb and diamond-based 2D sandwich architected materials fail and fracture?

(ii) What aspects of the fracture process are reproducible?

(iii) What effect does micro-architecture have on fracture and failure? (iv) What are the differences between dynamic and static loading for these kinds of architected sandwich structures?

1.1 Mechanical Behaviour of Lattice Structures

Two important parameters control the internal and external mechanical behaviour of a structure: material and geometry. Initial interest in metallic and polymeric foams in the late 1990s led to the investigation of the structural stability of individual foam struts. This led to the classification of strut-based cells into two categories based on how they deform: a mechanism or a structure [15]. When load is applied to a mechanism, bending initiates in each strut and the whole frame fails from post-flexural yield effects   a deformation mode termed bending-dominated. When load is applied to a structure, struts become axially loaded, with the dominant loading type being axial termed stretch-dominated deformation. Since bars in tension or compression are generally stiffer than those in bending, stretch-dominated structures are generally stiffer than bending-dominated counterparts, with the difference in stiffness potentially reaching a factor of three at a relative density of 0.1 [15].

The threshold for necessary stability in a lattice is governed by Maxwell's criterion, which computes a metric M given the number of struts b and joints j: $M = b - 2j + 3$ for 2D structures and $M = b - 3j + 6$ for 3D structures. When $M < 0$ the lattice is under-constrained; $M = 0$ indicates a rigid framework; $M > 0$ indicates an over-constrained structure [16].

It is also important to be able to predict, to some extent, the behaviour of sandwich lattice cores undergoing large-scale plastic distortion. Calladine and English patterned the responses of most structures into two idealised types: Type I and Type II [27]. Type I load response is characterised by an initial small elastic slope and an eventual plateau or shallow increase in force over increased deformation, with energy absorbed increasing steadily over prolonged deformation. For Type II structures, the load response is characterised by a high initial load and high stiffness before a decline as failure sets in, with energy response showing an initial steep curve that eventually plateaus [27].

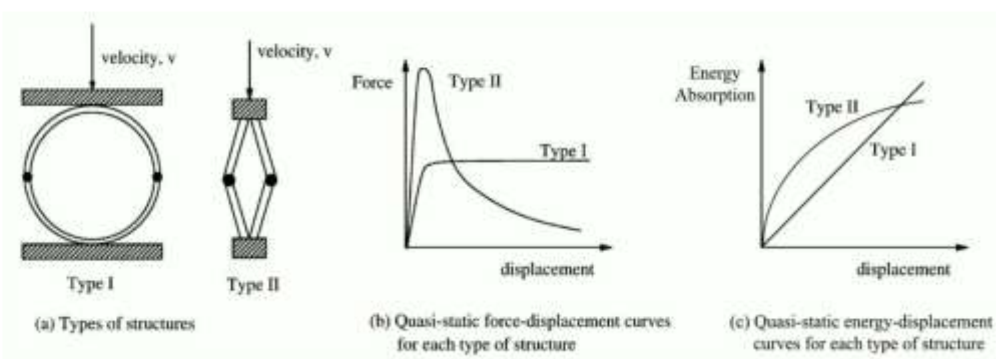

Figure 1. Description of Quasi-Static Response in the Two Idealised Types of Structure [27].

1.2 Sandwich Architected Structures

A sandwich structure consists of three layers: a top face plate, a middle core, and a bottom face plate [22]. Sandwich structures have played a vital role in structural, automotive, and aerospace industries because of their attractive application profile: a high stiffness-to-weight ratio, high energy absorption, and heat and sound dissipation [25]. The cellular core can be made from any geometrical topology, not limited to

© AUG 2023 | IRE Journals | Volume 7 Issue 2 | ISSN: 2456-8880
DOI: https://doi.org/10.64388/IREV7I2-1718338

2D (extruded in the third dimension, 2.5D) or 3D. The type of cellular geometry used and the orientation of the core determine how the sandwich structure performs under loading [17], [19].

With increased interest in the mechanical behaviour of pseudo-periodic architected materials such as functionally graded structures and hybrid lattices, experimental studies investigating the effect of cell gradation on fundamental topologies are needed [30]. This study addresses that gap by including functionally graded variants for both honeycomb and diamond topologies, where the vertical heights of the unit cells are graded according to a prescribed mathematical function [24].

II. MATERIALS AND METHODS

2.1 Specimen Design and Architecture

There are two primary topologies considered in this study:

(i) Honeycomb (hexagonal lattice): consists of tessellated unit cells of hexagons.

(ii) Diamond-celled lattice: a reoriented square lattice.

Parametric variation was achieved by changing the angle θ in the unit cell of each topology. For honeycomb, the angular variations were 15°, 30°, and 45°; for diamond, 45°, 90°, and 120°. In addition, a functionally graded variant was included for each topology, in which the vertical cell height was graded across the core thickness using a prescribed growth function. The unit cell wall length (L_unit) was fixed at 12 mm and wall thickness (t) at 1 mm for all angular honeycomb and diamond specimens. Figure 2 shows the unit cell design parameters for both topologies.

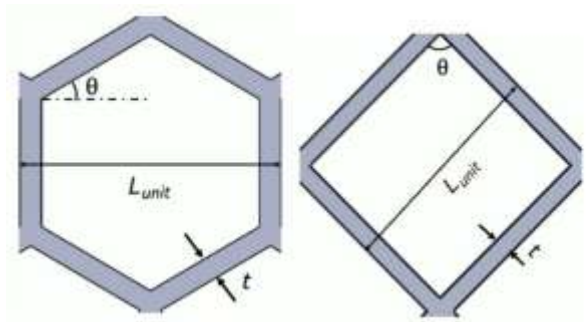

Figure 2. Unit cell design of honeycomb (left) and diamond (right) lattices, showing the controlled angle θ, unit cell length L_unit, and wall thickness t.

Specimens undergoing local compression (3-point bending) were designed as sandwich beams (135 × 25 × 48 mm), those undergoing quasi-static uniform compression and low-velocity impact were designed as sandwich panels (80 × 80 × 48 mm). Face plate thickness was fixed at 4 mm and core thickness at 40 mm for all specimens. All specimens except the functionally graded honeycomb were designed in SOLIDWORKS 2021; the functionally graded honeycomb specimens were designed in Blender v3.3.1 to accurately implement the grading functions. Figure 3 shows the design of the diamond sandwich panels.

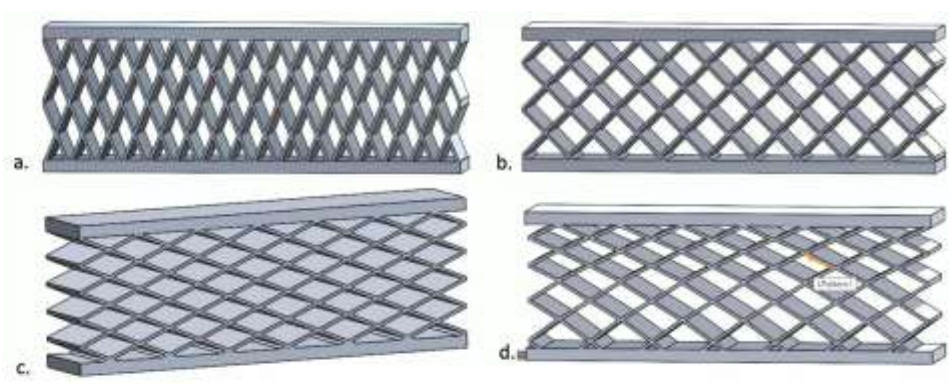

Figure 3. Diamond sandwich panel designs for: (a) 45°, (b) 90°, (c) 120°, and (d) Functionally Graded configurations.

© AUG 2023 | IRE Journals | Volume 7 Issue 2 | ISSN: 2456-8880
DOI: https://doi.org/10.64388/IREV7I2-1718338

2.2 Material and Manufacturing

A UV-curable brittle photopolymer resin (ANYCUBIC Basic Resin) was selected as the constituent material. The brittle failure mode of this resin post-curing was essential for the observation of specimen fracture [5], [6]. The resin composition is 60% epoxy resins, 35% (1-methyl-1,2-ethanediyl)bis[oxy(methyl-2,1-ethanediyl)] diacrylate, and 5% hydroxycyclohexyl phenyl ketone. Specimens were manufactured using an ANYCUBIC Photon Mono X LCD resin printer, washed in 99% isopropyl alcohol for 5–10 minutes, and cured for 2 minutes in an ANYCUBIC UV curing station. Parts were oriented at 45° during printing to minimise the pulling area against the vat film, reducing warping [10].

A total of 120 specimens were fabricated: 5 replicates × 8 topology/variation combinations × 3 loading conditions. Initial CAD properties (dimensions and density) were used as the reference point for all comparative analyses, as manufacturing tolerances introduce small dimensional variations in the final cured parts [21], [23].

2.3 Bulk Material Characterisation

The mechanical properties of the UV-cured ANYCUBIC resin were characterised prior to structural testing [3]. Three-point bending tests followed ASTM C1161-13 (prism samples: 140 × 6 × 8 mm) and used a 100 mm span length at 5 mm/min. Compressive properties were obtained per ASTM D695-15 (samples: 12.7 × 12.7 × 25.4 mm) at 2 mm/min. Tensile properties were obtained per ASTM D638-14 (dogbone specimens) at 5 mm/min. Five specimens were tested for each configuration. All tests were conducted on a Newton Universal Testing Machine (UTM). The bulk material properties are summarised in Table 1.

The average flexural strength was 25.193 ± 2.240 MPa and average flexural stiffness was 0.608 ± 0.074 GPa. Average compressive strength was 55.785 ± 6.474 MPa with compressive stiffness of 1.048 ± 0.069 GPa. The compressive stress-strain data showed high consistency across specimens, with standard deviations within 12% of the respective means. Figure 4 shows the compressive stress-strain response, which displays a consistent brittle failure at the peak stress with minimal post-peak ductility.

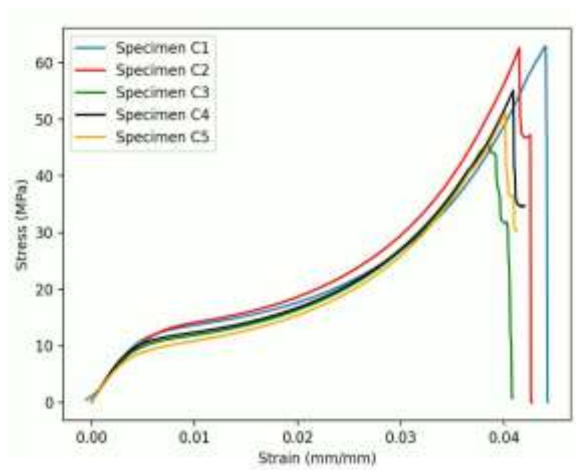

Figure 4. Compression Stress vs. Strain of the five tested ANYCUBIC resin specimens, showing consistent brittle failure behaviour.

Table 1. Mechanical properties of bulk UV-cured ANYCUBIC resin. (*Supplier data)

Mechanical Property	Values	Test Standard
Tensile Strength (MPa)	22.192 ± 2.317	ASTM D638-14
Tensile Modulus (GPa)	0.528 ± 0.040	ASTM D638-14
Flexural Strength (MPa)	25.193 ± 2.240	ASTM C1161-13
Flexural Modulus (GPa)	0.608 ± 0.074	ASTM C1161-13
Compressive Strength (MPa)	55.785 ± 6.474	ASTM D695-15
Compressive Modulus (GPa)	1.048 ± 0.069	ASTM D695-15

Mechanical Property	Values	Test Standard
Density (g/cm³)*	1.250	Supplier data
Viscosity (mPa·s)*	200	Supplier data

2.4 Testing Procedures

Three experimental methods were employed, each with unique setups and fixtures, and all performed at room temperature.

2.4.1 Three-Point Bending

The 3-point bending setup consisted of a loading nose and two support points spanning 100 mm. The displacement rate was 5 mm/min and specimens were deformed to 24 mm (50% of the beam depth). The Newton UTM machine crosshead was operated using the Newton software package.

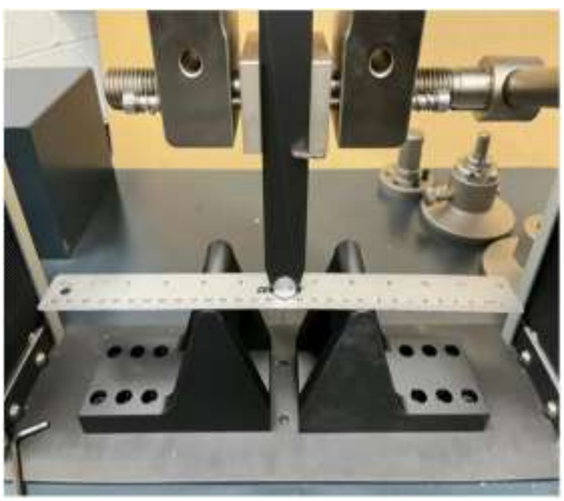

Figure 5. Three-point bending test setup showing the loading nose and two support points with 100 mm span.

2.4.2 Quasi-Static Compression

The compression test setup comprised two circular (116 mm diameter) steel plate fixtures. The displacement rate was 2 mm/min and panels were deformed to 20 mm (50% of the core depth). The crosshead was controlled using the Newton software package.

2.4.3 Low-Velocity Impact

The low-velocity impact setup consisted of a 3-inch diameter steel ball bearing (weight: 18 N) dropped from a height of 30 cm into a 3-inch pipe and onto a circular disc placed atop a pressure sensor. A National Instruments myDAQ data acquisition system acquired voltage readings from the sensor, processed through an inverting amplifier with a 10 kΩ resistor. A Phantom v5.2 high-speed camera recorded the fracture process. Note that the measured force represents transmitted force at the sensor location, not the direct impact force at the panel centre.

Figure 6. Post-impact specimen showing the characteristic fracture pattern at the impact point centre, with crack propagation to the face sheet.

2.4.4 Digital Image Correlation (DIC)

Selected specimens were prepared for 2D Digital Image Correlation (DIC) analysis to obtain full-field displacement and strain data on the front-facing plane of the specimen. Specimens were painted with matte white paint using a roller, followed by application of a dense black speckle pattern using a toothbrush. Image capture was performed using a Sony A7IV camera with a 35 mm lens, and correlation analysis was performed using the open-source DICe (Digital Image Correlation engine) software developed by Sandia Laboratories. Strain values obtained were global (not local to individual strut axes).

III. RESULTS

3.1 Three-Point Bending Results

This section covers the structural performance and fracture process of each architected sandwich specimen category under local compressive loading. Each specimen was deformed to 50% of the beam depth (24 mm). Post-failure images were taken immediately after face sheet failure to observe fracture propagation through the beam cores. The load response of all honeycomb and most diamond variations conformed to a Type II structure response characterised by a high initial peak followed by successive smaller peaks during densification (Figure 7).

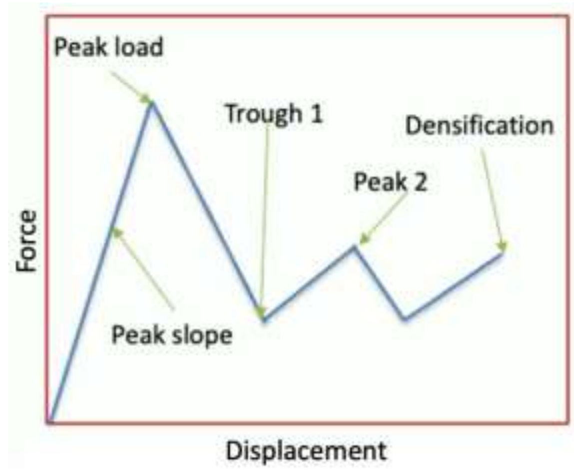

Figure 7. Schematic of the observed Type II load response pattern in honeycomb and 45°/90° diamond sandwich beams under 3-point bending, showing peak load, trough, secondary peak, and densification phases.

3.1.1 Honeycomb Variations

For the 15° honeycomb category, the average peak load was 413.46 ± 31.22 N with an average energy absorption of 5.019 ± 0.423 J. The fracture process showed two consistent paths: a 180°/straight path starting at the bottom corner of the beam core (primary, red), and an opposite 180° path from the top row (secondary, blue), with both converging at the beam centreline beneath the loading nose. Post-failure images showing these consistent patterns are presented in Figure 8. DIC strain analysis confirmed that compressive and shear strains dominated in the core before failure, with core shear being the primary failure mode.

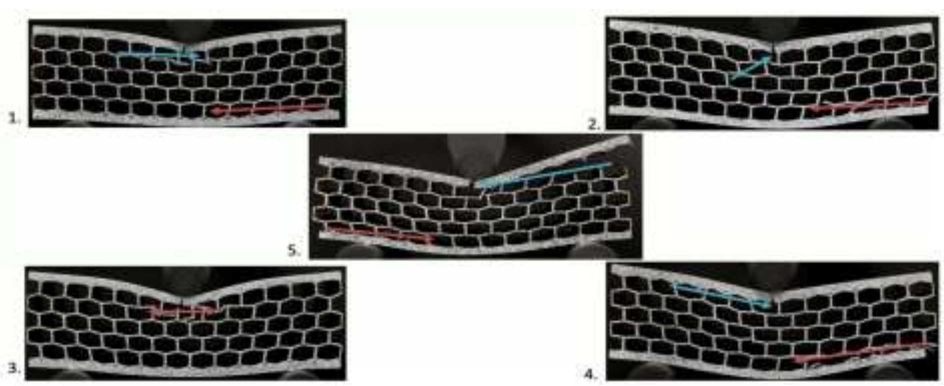

Figure 8. Post-failure images of the five tested 15° honeycomb sandwich beams showing two consistent fracture paths: a 180° path from the bottom row (red arrows) and an opposing 180° path from the top row (blue arrows).

For the 30° variation, average peak load was 324.75 ± 24.29 N with 3.521 ± 0.377 J energy absorbed. Two consistent fracture paths were again observed: a primary 120°/obtuse-angle path ascending from the bottom corner to the top centre, and a secondary 180° path from the second row. The 45° variation recorded 315.24 ± 5.61 N peak load and 3.651 ± 0.248 J; no consistent fracture pattern was observed, attributed to asymmetry in the core design and loading nose position not directly engaging a strut beneath the face sheet. The functionally graded variation achieved 399.90 ± 34.07 N peak load with 4.979 ± 0.860 J, exhibiting a primary 120° crack path from the bottom row for both bending and compression specimens. Core shear was the dominant failure mode across all honeycomb variations, with minor buckling observed in some strut members.

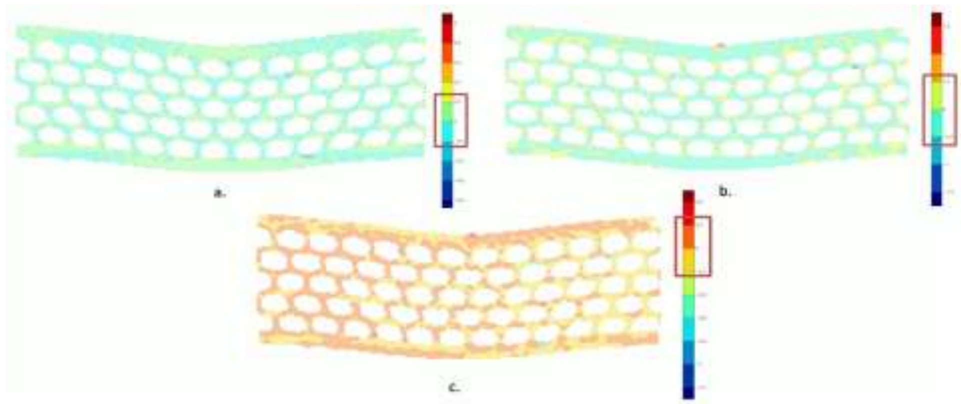

Figure 9. DIC strain contour maps for the 15° honeycomb specimen 2 immediately before initial core failure: (a) Lateral strain (εxx), (b) Compressive strain (εyy), (c) Shear strain (εxy). Shear strain is the dominant field, confirming core shear as the primary failure mode.

3.1.2 Diamond Variations

The 45° diamond variation recorded the highest bending performance of all categories, with an average peak load of 1126.47 ± 263.87 N and energy absorption of 7.964 ± 2.367 J. While face sheet failure was present, there was no significant large-scale damage in the core   only the onset of buckling with lateral deflection at the centre. Lateral strain dominated in DIC analysis, confirming buckling as the primary failure mode.

The 90° variation recorded 685.05 ± 132.35 N and 6.364 ± 2.388 J; no consistent fracture pattern was observed, attributed to the loading nose not engaging the core directly beneath the face sheet. The 120° variation exhibited a Type I structure response, with a slow but steady rise in load over the full displacement range, recording an average peak load of 339.01 ± 24.90 N and energy absorption of 5.328 ± 0.202 J. Large-scale fracture was absent but significant localised deformation occurred in the 1st, 2nd, and 3rd rows in an accordion-like pattern. The functionally graded variation also showed a Type I response (253.21 ± 75.73 N; 4.922 ± 0.404 J), with localised deformation in the 1st and 2nd rows and markedly less deformation in subsequent rows   demonstrating the tunability effect of functionally graded structures where compliance can be selectively programmed into specific core regions. Results are summarised in Table 2.

Table 2. Summary of Average Peak Load and Absorbed Energy for Sandwich Beams Under 3-Point Bending.

Honeycomb			Diamond		
Category	Av. Peak Load (N)	Av. Energy Absorbed (J)	Category	Av. Peak Load (N)	Av. Energy Absorbed (J)
15°	413.46 ± 31.22	5.019 ± 0.423	45°	1126.47 ± 263.87	7.964 ± 2.367
30°	324.75 ± 24.29	3.521 ± 0.377	90°	685.05 ± 132.35	6.364 ± 2.388
45°	315.24 ± 5.61	3.651 ± 0.248	120°	339.01 ± 24.90	5.328 ± 0.202
Func. Graded	399.90 ± 34.07	4.979 ± 0.860	Func. Graded	253.21 ± 75.73	4.922 ± 0.404

3.2 Quasi-Static Compression Results

This section covers the performance and fracture process of architected sandwich panels under uniform compressive loading. Each specimen was deformed to 20 mm (50% of the core depth). Images were captured at the 10 mm (25% core deformation) mark to highlight fracture propagation before densification commenced.

3.2.1 Honeycomb Variations

The 15° honeycomb variation recorded an average peak load of 1713.70 ± 446.45 N with energy absorption of 15.791 ± 3.720 J. The response was classified as a partial Type II, as subsequent peaks were equal to or higher than the initial peak across all five specimens. The primary fracture path was a step-like process starting from the bottom row and ascending to the first row   a pattern consistently reproduced across specimens. The 30° variation recorded 1778.61 ± 110.21 N and 13.775 ± 1.074 J (Type II), though no consistent fracture pattern was observed. The 45° variation showed the highest load consistency (2283.27 ± 52.34 N; 14.323 ± 1.455 J), also without a reproducible fracture pattern.

The functionally graded honeycomb variation achieved the highest peak load of any honeycomb category (2800.81 ± 82.41 N; 24.015 ± 0.913 J), with a consistent 120° fracture path from the bottom row ascending to the opposite end of the top row. Core shear was the primary failure mode across all honeycomb compression categories, with the near-horizontal struts shearing more than the vertical ones, facilitating the step-like collapse pattern.

3.2.2 Diamond Variations

The 45° diamond variation recorded peak loads of 8455.89 ± 138.33 N with 54.637 ± 1.151 J energy absorbed the highest values recorded for any category across all experiment types. A 180° straight fracture path through the middle row was consistently observed. Buckling was the primary failure mode, driven by the steep angle of the struts. Figure 10 shows post-failure images of the 45° diamond panels at 25% core deformation, clearly illustrating the through-row fracture path.

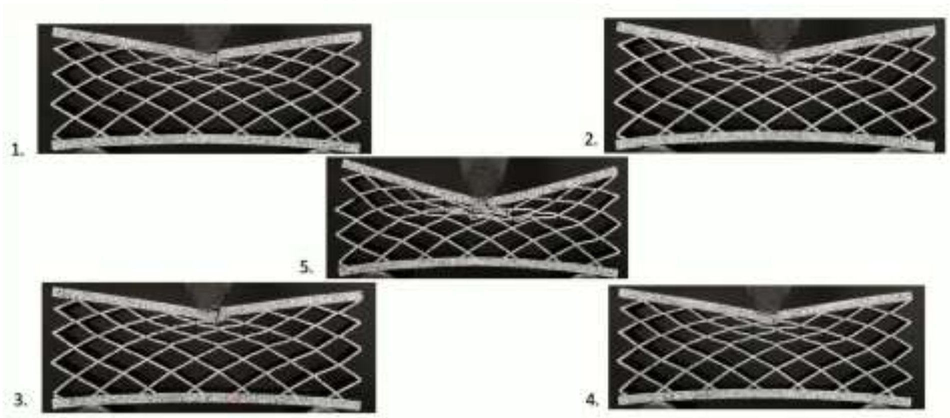

Figure 10. Post-failure images of the five 45° diamond sandwich panels at 25% core deformation. The primary fracture path is a 180° line through the middle (second) row of the core, with the entire row collapsing due to strut buckling.

The 90° variation recorded 2406.92 ± 164.84 N and 17.498 ± 1.469 J (Type II), with primary fracture paths of 120° from the top row and a secondary 180° path through the bottom row. Buckling again dominated. The 120° variation showed a Type I response with the lowest peak load (408.19 ± 82.57 N) and 8.746 ± 0.273 J absorbed energy; significant but localised deformation occurred in the middle row, with minimal fracture. The functionally graded variation also showed Type I behaviour (509.28 ± 70.65 N; 10.036 ± 0.724 J), with deformation concentrated in the upper rows, reinforcing the tunability advantage observed in bending. A full summary of compression results is given in Table 3.

Table 3. Summary of Average Peak Load and Absorbed Energy for Sandwich Panels Under Quasi-Static Compression.

Honeycomb			Diamond		
Category	Av. Peak Load (N)	Av. Energy Absorbed (J)	Category	Av. Peak Load (N)	Av. Energy Absorbed (J)
15°	1713.70 ± 446.45	15.791 ± 3.720	45°	8455.89 ± 138.33	54.637 ± 1.151
30°	1778.61 ± 110.21	13.775 ± 1.074	90°	2406.92 ± 164.84	17.498 ± 1.469
45°	2283.27 ± 52.34	14.323 ± 1.455	120°	408.19 ± 82.57	8.746 ± 0.273
Func. Graded	2800.81 ± 82.41	24.015 ± 0.913	Func. Graded	509.28 ± 70.65	10.036 ± 0.724

3.3 Low-Velocity Impact Results

This section covers the force-time response and fracture process of sandwich panels under a low-velocity impact load dropped from 30 cm. Unlike the static tests, this experiment focused on impulse force values and fracture patterns observed in the milliseconds after impactor contact. All tested specimens exhibited a consistent initial impulse peak followed by oscillatory decay.

3.3.1 Honeycomb Variations

The 15° variation recorded an average peak impact load of 1698.62 ± 200.29 N, with fracture limited to the 1st and 2nd rows emanating from the impact centre. The 30° variation showed a similar peak (1741.61 ± 187.32 N), with fracture also limited to the 1st and 2nd rows. The 45° variation recorded 1926.47 ± 68.17 N with high force consistency; only 2 of 5 specimens fractured, with fracture propagating to the bottom corner in the one that did. The functionally graded variation achieved 1945.27 ± 43.44 N the highest among honeycomb categories with fracture constrained to the central core region. Face sheet deflection was less pronounced in the 45° and functionally graded categories compared to the 15° and 30° variations.

3.3.2 Diamond Variations

The 45° diamond variation achieved the highest average peak impact load of any category: 2447.08 ± 42.38 N with exceptional consistency (Figure 11). Fracture was limited to the 1st row only, occurring only at the direct impact point and not propagating to the front plane. There was negligible face sheet deflection, reflecting the high stiffness of this configuration.

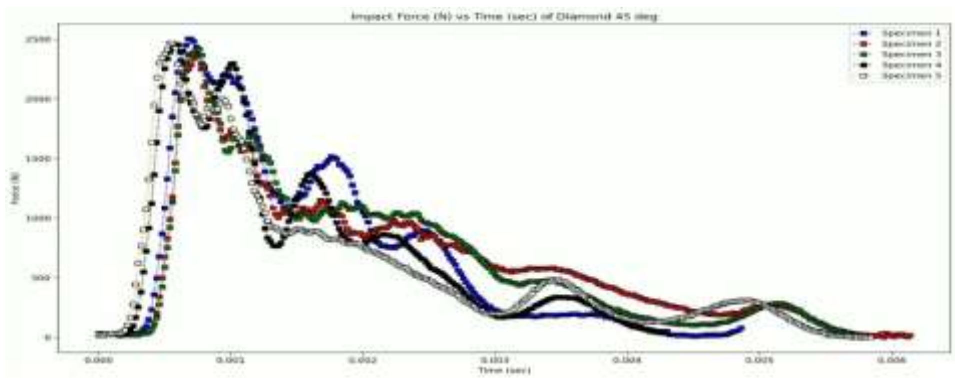

Figure 11. Impact Force (N) vs. Time (s) for the five 45° diamond sandwich panels. Peak loads exceed 2,400 N with high reproducibility across specimens, and the broad plateau reflects energy dissipation by the core.

The 90° variation recorded 1736.73 ± 295.31 N, with fracture limited to the 1st and 2nd rows and little face sheet deflection. In marked contrast, the 120° diamond variation recorded only 761.02 ± 27.30 N by far the lowest of all categories. The broader spread of time under impact force indicates that the compliant 120° core absorbed much of the impact energy, resulting in large-scale deformation rather than fracture (Figure 12). Four of five specimens showed little to no fracture but experienced significant face sheet and core deformation.

© AUG 2023 | IRE Journals | Volume 7 Issue 2 | ISSN: 2456-8880
DOI: https://doi.org/10.64388/IREV7I2-1718338

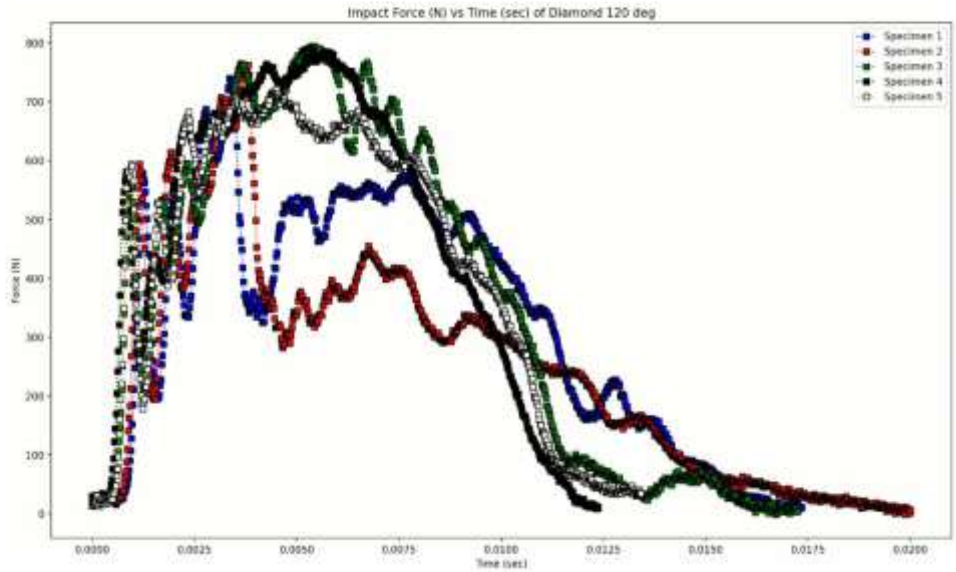

Figure 12. Impact Force (N) vs. Time (s) for the five 120° diamond sandwich panels, showing substantially lower peak loads (~760 N on average) and a broader time profile compared to the 45° diamond, indicating superior impact energy absorption.

The functionally graded diamond variation recorded 775.35 ± 102.59 N, comparable to the 120° category. More fracturing occurred than in the 120° category, concentrated in the face sheet and upper row edges, while the stiffer lower rows resisted deformation again demonstrating the programmable tunability of functionally graded designs. A summary of all impact results is provided in Table 4.

Table 4. Summary of Average Peak Impact Load and Fracture Characteristics for All Sandwich Panels Under Low-Velocity Impact.

Topology	Category	Av. Peak Load (N)	Fracture Pattern
Honeycomb	15°	1698.62 ± 200.29	Limited to 1st & 2nd rows
Honeycomb	30°	1741.61 ± 187.32	Limited to 1st & 2nd rows
Honeycomb	45°	1926.47 ± 68.17	Propagates to bottom corner
Honeycomb	Func. Graded	1945.27 ± 43.44	Constrained within center
Diamond	45°	2447.08 ± 42.38	Limited to 1st row; no deflection
Diamond	90°	1736.73 ± 295.31	Limited to 1st & 2nd rows
Diamond	120°	761.02 ± 27.30	Little fracture; large deformation
Diamond	Func. Graded	775.35 ± 102.59	Fracture in 1st & 2nd rows

IV. DISCUSSION

4.1 Failure Modes and Reproducibility

The results demonstrate that the dominant failure mode for all honeycomb variations under both 3-point bending and quasi-static compression was core shear, consistent with prior literature on honeycomb lattice response under in-plane loading [28], [29]. Buckling was a secondary mode and was more pronounced in the in-plane direction during compression. For the diamond topology, the dominant failure mode shifted with angular variation: 45° and 90° variations exhibited buckling-dominated failure, while the 120° and functionally graded variations showed bending-dominated deformation with minimal fracture a transition attributable to the increasingly obtuse angle changing the effective strut connectivity and reducing the Maxwell stability criterion value toward the under-constrained regime [15], [16].

Reproducibility was high for the load response in both honeycomb and diamond variations under static loading, with standard deviations in peak load consistently within 12–25% of the mean across five replicates. Fracture paths, however, were only reproducible for a subset of categories. The 15° honeycomb, 30° honeycomb, functionally graded honeycomb, 45° diamond (compression), 90° diamond (compression), and 15° diamond (compression) categories exhibited recognisable and consistently repeated fracture paths across specimens. Categories without repeatable patterns (honeycomb 30° compression, honeycomb 45°, diamond 45° and 90° bending) appear to be sensitive to the initial contact between the loading fixture and the core struts a limitation driven by the lack of enforced core symmetry in the specimen design.

4.2 Effect of Micro-Architecture on Performance

Angular variation produced markedly different structural performance profiles within each topology. For honeycomb, the primary metric that varied across angular categories was the peak load, with the 15° variation achieving the highest value (413.46 N under bending; 1713.70 N under compression) and the 45° variation the lowest in bending (315.24 N). The energy absorption values were similar across honeycomb categories under bending, suggesting that the angle primarily affects strength (stiffness and peak load) rather than total energy dissipation capacity.

The sensitivity of the diamond topology to angular changes was far more pronounced. The 45° diamond variation recorded a bending peak load of 1126.47 N approximately 3× the corresponding honeycomb values while the 120° variation recorded 339.01 N under bending, a 70% reduction from the 45° configuration. The 45° diamond configuration is the most suitable for high-stiffness, low-deformation applications, while the 120° and functionally graded diamond configurations are optimal for impact absorption and compliant energy dissipation applications [26], [27].

The functionally graded structures demonstrated the most practically significant finding of the study: a tunability effect where structural compliance can be allocated to specific core regions. Under both bending and compression, deformation was concentrated in the more compliant (larger-angle, lower-row) regions, leaving the stiffer regions largely undamaged. This multi-zone response is unique to pseudo-periodic architectures and cannot be achieved with uniform lattice designs [12], [30].

4.3 Static vs. Dynamic Loading

All specimens achieved their highest peak loads under quasi-static compression and lowest under 3-point bending. This trend confirms that the uniformly distributed loading condition is more efficient in engaging the full core volume, while local loading concentrates stress beneath the nose and causes earlier core failure. Under low-velocity impact, the force response was less consistent in shape than under static loading, particularly for honeycomb categories, and no recognisable load-time patterns emerged within categories.

The most striking static-versus-dynamic contrast was observed in the diamond topology: the 45° variation recorded the highest transmitted impact force (2447.08 N) consistent with its stiffness-driven static performance while the 120° variation recorded the lowest (761.02 N). The lower peak transmitted force in the 120° case indicates that more impact energy was absorbed by the compliant core rather than transmitted to the sensor platform. The broader force-time impulse

© AUG 2023 | IRE Journals | Volume 7 Issue 2 | ISSN: 2456-8880
DOI: https://doi.org/10.64388/IREV7I2-1718338

profile for the 120° variation (Figure 12 vs. Figure 11) provides additional confirmation of this energy-absorption mechanism.

The assumption from Calladine and English [27] that Type I and Type II structures retain their characteristic responses under impact loading (provided the velocity does not alter the quasi-static collapse mode) was largely validated. Type II honeycomb and 45°/90° diamond categories showed sharp impulse peaks in impact, consistent with their high initial stiffness. Type I structures (120° and functionally graded diamond) showed the lower, broader impulse profiles corresponding to their progressive compliance.

4.4 Digital Image Correlation Validation

DIC analysis provided full-field strain validation of the visually identified failure modes. For the honeycomb categories where correlation was successful, shear strain (εxy) was the dominant field immediately preceding core failure, confirming core shear as the primary failure mechanism. For the 45° diamond category under bending, lateral strain (εxx) dominated consistent with the onset of buckling-driven lateral deflection observed in post-failure images. The y-axis displacement maps from DIC also provided quantitative data useful for future simulation validation efforts. Figure 13 shows a representative DIC y-displacement map for the functionally graded honeycomb specimen, illustrating the gradient in vertical displacement across the core maximum at the loading nose contact point and decaying toward the supports.

Figure 13. DIC y-axis displacement map (mm) for a functionally graded honeycomb specimen under 3-point bending, showing the displacement gradient from the loading nose contact point (red, ~4.41 mm) to the support regions (blue, ~0 mm).

V. CONCLUSION

This study presents a systematic experimental investigation of failure modes and deformation patterns in 2D honeycomb and diamond sandwich architected structures manufactured via additive manufacturing and tested under three loading conditions. The following conclusions can be drawn:

(1) Core shear was the dominant failure mode across all honeycomb variations under both bending and compression, while buckling dominated for 45° and 90° diamond variations. The 120° and functionally graded diamond variations exhibited bending-dominated deformation with minimal fracture.

(2) Load response reproducibility was high under static loading. Recognisable Type II patterns were found in honeycomb and lower-angle diamond variations; Type I responses were observed in 120° and functionally graded diamond configurations, consistent with the theoretical predictions of Calladine and English [27].

(3) Repeatable fracture paths including 180° straight and 120° oblique crack propagation lines were identified for several categories under both bending and compression, providing a reference dataset for

simulation validation. Categories without consistent patterns were attributed to lack of core symmetry and loading nose positioning relative to core struts.

(4) The 45° diamond variation achieved the highest strength and stiffness under all three loading conditions, making it the most suitable configuration for high-stiffness structural applications. The 120° diamond variation demonstrated the highest impact energy absorption, with the lowest transmitted impact force and the largest deformation without fracture.

(5) Functionally graded structures exhibited a programmable tunability effect, with compliance and deformation concentrated in specific, targeted core regions. This multi-zone behaviour distinguishes pseudo-periodic architectures from uniform lattice designs and represents a significant advantage for application-specific structural design.

Future work should enforce core symmetry in specimen design to improve fracture pattern reproducibility, and should introduce density constraints to enable equitable comparative analysis across topology types. Extension of this experimental dataset to enable model validation for finite element simulations of sandwich lattice failure is recommended.

REFERENCES

[1] H. com Editors, "Iron Age," HISTORY. https://www.history.com/topics/pre-history/iron-age (accessed Nov. 08, 2022).

[2] J. R. Greer and V. S. Deshpande, "Three-dimensional architected materials and structures: Design, fabrication, and mechanical behavior," MRS Bull., vol. 44, no. 10, pp. 750–757, Oct. 2019, doi: 10.1557/mrs.2019.232.

[3] D. Ionesi and L. Ciobanu, “EVALUATION OF TENSILE BEHAVIOR OF RAW MATERIALS USED FOR COMPOSITES REINFORCEMENT,” Jun. 2013.

[4] N. A. Fleck, V. S. Deshpande, and M. F. Ashby, "Micro-architectured materials: past, present and future," Proc. R. Soc. Math. Phys. Eng. Sci., vol. 466, no. 2121, pp. 2495–2516, Jun. 2010, doi: 10.1098/rspa.2010.0215.

[5] L. Guo, X. Ou, S. Ni, Y. Liu, and M. Song, “Effects of carbon on the microstructures and mechanical properties of FeCoCrNiMn high entropy alloys,” *Mater. Sci. Eng. A*, vol. 746, pp. 356–362, Feb. 2019, doi: 10.1016/j.msea.2019.01.050.

[6] N. V. Stepanova and A. A. Razumakov, “The effect of doping with copper and aluminum on structure, mechanical and friction properties of steel,” in *Ifost*, Jun. 2013, pp. 240–242. doi:10.1109/IFOST.2013.6616977

[7] M. F. Ashby, "The properties of foams and lattices," Philos. Trans. R. Soc. Math. Phys. Eng. Sci., vol. 364, no. 1838, pp. 15–30, Jan. 2006, doi: 10.1098/rsta.2005.1678.

[8] L. J. Gibson and M. F. Ashby, Cellular Solids: Structure and Properties, 2nd ed. Cambridge: Cambridge University Press, 1997. doi: 10.1017/CBO9781139878326.

[9] M. F. Ashby and Y. J. M. Bréchet, "Designing hybrid materials," Acta Mater., vol. 51, no. 19, pp. 5801–5821, Nov. 2003, doi: 10.1016/S1359-6454(03)00441-5.

[10] R. Gmeiner *et al.*, “Additive Manufacturing of Bioactive Glasses and Silicate Bioceramics,” *J. Ceram.Sci. Technol.*, vol. 6, pp. 75–86, Jun. 2015, doi: 10.4416/JCST2015-00001.

[11] J. Song *et al.*, “Octet-truss cellular materials for improved mechanical properties and specific energy absorption,” *Mater. Des.*, vol. 173, p. 107773, Apr. 2019, doi: 10.1016/j.matdes.2019.107773.

[12] N. Kladovasilakis, K. Tsongas, D. Karalekas, and D. Tzetzis, "Architected Materials for Additive Manufacturing: A Comprehensive Review," Materials, vol. 15, no. 17, Jan. 2022, doi: 10.3390/ma15175919.

[13] D. Bhate, C. A. Penick, L. A. Ferry, and C. Lee, “Classification and Selection of Cellular Materials in Mechanical Design: Engineering and Biomimetic Approaches,” *Designs*, vol. 3, no. 1, Art. no. 1, Mar. 2019, doi: 10.3390/designs3010019.

[14] I. E. Ramirez-Chavez, D. Anderson, R. Sharma, C. Lee, and D. Bhate, “A Classification of Aperiodic Architected Cellular Materials,” *Designs*, vol. 6, no. 4, Art. no. 4, Aug. 2022, doi: 10.3390/designs6040063.

[15] V. S. Deshpande, M. F. Ashby, and N. A. Fleck, "Foam topology: bending versus stretching dominated architectures," Acta Mater., vol. 49, no. 6, pp. 1035–1040, Apr. 2001, doi: 10.1016/S1359-6454(00)00379-7.

[16] J. C. Maxwell, "XLV. On reciprocal figures and diagrams of forces," Lond. Edinb. Dublin Philos. Mag. J. Sci., vol. 27, no. 182, pp. 250–261, Apr. 1864, doi: 10.1080/14786446408643663.

[17] H. N. G. Wadley, N. A. Fleck, and A. G. Evans, "Fabrication and structural performance of periodic cellular metal sandwich structures," Compos. Sci. Technol., vol. 63, no. 16, pp. 2331–2343, Dec. 2003, doi: 10.1016/S0266-3538(03)00266-5.

[18] J. Banhart and H.-W. Seeliger, "Aluminium Foam Sandwich Panels: Manufacture, Metallurgy and Applications," Adv. Eng. Mater., vol. 10, no. 9, pp. 793–802, 2008, doi: 10.1002/adem.200800091.

[19] S. M. Zaharia, L. A. Enescu, and M. A. Pop, "Mechanical Performances of Lightweight Sandwich Structures Produced by Material Extrusion-Based Additive Manufacturing," Polymers, vol. 12, no. 8, Aug. 2020, doi: 10.3390/polym12081740.

[20] N. Kladovasilakis et al., "Experimental and Computational Investigation of Lattice Sandwich Structures Constructed by Additive Manufacturing Technologies," J. Manuf. Mater. Process., vol. 5, no. 3, Sep. 2021, doi: 0.3390/jmmp5030095.

[21] A. Maguire, N. Pottackal, M. A. S. R. Saadi, M. M. Rahman, and P. M. Ajayan, "Additive manufacturing of polymer-based structures by extrusion technologies," *Oxf. Open Mater. Sci.*, vol. 1, no. 1, p. itaa004, Jan. 2021, doi: 10.1093/oxfmat/itaa004.

[22] I. Maskery *et al.*, "A mechanical property evaluation of graded density Al-Si10-Mg lattice structures manufactured by selective laser melting," *Mater. Sci. Eng. A*, vol. 670, pp. 264–274, Jul. 2016, doi: 10.1016/j.msea.2016.06.013.

[23] M. a. S. R. Saadi *et al.*, "Direct Ink Writing: A 3D Printing Technology for Diverse Materials," *Adv.Mater.*, vol. 34, no. 28, p. 2108855, 2022, doi: 10.1002/adma.202108855.

[24] C. M. Spadaccini, "Additive manufacturing and processing of architected materials," *MRS Bull.*, vol.44, no. 10, pp. 782–788, Oct. 2019, doi: 10.1557/mrs.2019.234.

[25] F. Zhu, G. Lu, D. Ruan, and Z. Wang, "Plastic Deformation, Failure and Energy Absorption of Sandwich Structures with Metallic Cellular Cores," Int. J. Prot. Struct., vol. 1, no. 4, pp. 507–541, Dec. 2010, doi: 10.1260/2041-4196.1.4.507.

[26] H. Yazdani Sarvestani, A. H. Akbarzadeh, A. Mirbolghasemi, and K. Hermenean, "3D printed meta-sandwich structures: Failure mechanism, energy absorption and multi-hit capability," Mater. Des., vol. 160, pp. 179–193, Dec. 2018, doi: 10.1016/j.matdes.2018.08.061.

[27] "Strain-rate and inertia effects in the collapse of two types of energy-absorbing structure," Int. J. Mech. Sci., vol. 26, no. 11–12, pp. 689–701, Jan. 1984, doi: 10.1016/0020-7403(84)90021-3.

[28] T. Li and L. Wang, "Bending behavior of sandwich composite structures with tunable 3D-printed core materials," Compos. Struct., vol. 175, pp. 46–57, Sep. 2017, doi: 10.1016/j.compstruct.2017.05.001.

[29] S. Hou, T. Li, Z. Jia, and L. Wang, "Mechanical properties of sandwich composites with 3d-printed auxetic and non-auxetic lattice cores under low velocity impact," Mater. Des., vol. 160, pp. 1305–1321, Dec. 2018, doi: 10.1016/j.matdes.2018.11.002.

[30] H. Niknam and A. H. Akbarzadeh, "Graded lattice structures: Simultaneous enhancement in stiffness and energy absorption," Mater. Des., vol. 196, p. 109129, Nov. 2020, doi: 10.1016/j.matdes.2020.109129.